Journal of the Serbian Society for Computational Mechanics / Vol. 18 / No. 2, 2024 / pp 1-32 / original paper
(10.24874/jsscm.2024.18.02.01)

ENHANCEMENT OF THERMAL AND ENTROPY PERFORMANCE OF CPU HEATSINK USING HYBRID NANOFLUID UNDER NATURAL MAGNETOHYDRODYNAMIC CONVECTION

Melouka Benyamina[1*] [0000-0001-9689-2338] **and Abderrahim Mokhefi**[1,2] [0000-0002-2036-2186]

[1] National Polytechnic School of Oran Maurice Audin, Department of Mechanical Engineering, LaRTFM Laboratory, Oran, Algeria
e-mail**:** melouka.benyamina@enp-oran.dz, abderrahim.mokhefi@univ-bechar.dz
[2] Bechar University, Faculty of Sciences and Technology, Mechanics, Modeling and Experimentation Laboratory L2ME, B.P.417, 08000, Bechar, Algeria
e-mail: abderrahim.mokhefi@univ-bechar.dz
**corresponding author*

Abstract

The need for effective CPU cooling has become increasingly important with the growing demand for computing performance. In this paper, we numerically investigate the problem of active CPU cooling using hybrid nanofluids. The studied heatsink consists of a parallelepiped-shaped block filled with a hybrid nanofluid, crossed by four tubes through which a specialized liquid circulates within the CPU components. Our study focuses on elucidating the influence of CPU temperature, magnetic field, and its inclination, nanoparticle hybridization, and the spacing between the four tubes on the cooling capacity and entropy generation within the heatsink. The thermal phenomenon is governed by mass, momentum, and energy conservation equations. We employ finite element discretization using COMSOL Multiphysics 6.0 software to numerically solve these equations. The results show a significant enhancement in heat transfer using hybrid nanofluids, particularly with alumina nanoparticles, with a percentage increase of up to 15%. However, an increase in entropy generation is also observed. Furthermore, a widely spaced tube configuration is found to be particularly effective in terms of entropy, resulting in a cooling enhancement of up to 73%. It is noteworthy that the results of this research provide valuable data that enable the design of high-performance heatsinks of this type.

Keywords: central processor unit, heatsink, hybrid nanofluid, magnetic field, cooling, entropy

1. Introduction

With the rapid evolution of technology and the constant increase in computing power of CPUs, efficient heat dissipation has become a major concern in the field of computing and information technology. The accumulation of heat inside CPUs can lead to performance reduction, decreased component lifespan, and even system failures. Therefore, it is essential to implement effective cooling systems to maintain CPUs within acceptable temperature ranges (Siricharoenpanich et al., 2019).

Over the years, many approaches have been developed to enhance CPU cooling performance. Among these approaches, the use of nanofluids has garnered increasing interest due to their ability to improve heat transfer. Nanofluids are suspensions of nanoparticles in a base fluid, thereby providing a combination of advantages from different nanoparticle species suspended in a fluid (Keblinski et al., 2005; Buongiorno, 2006; Xie et al., 2002). Hybrid nanofluids are suspensions that combine the properties of different nanoparticle species in a base fluid. These suspensions offer unique advantages in terms of heat transfer and cooling performance. By mixing different nanoparticles, it is possible to leverage the specific characteristics of each species to optimize the performance of the nanofluid (Raj et al., 2019; Park and Jung, 2019).

Introducing the magnetohydrodynamic (MHD) effect in studies of electronic equipment cooling using nanofluids provides a more realistic and comprehensive approach, particularly for investigating CPU cooling using hybrid nanofluids. MHD allows the study of the interaction between the leaked magnetic field from this electronic equipment and the conductive fluid, which can have a significant impact on cooling performance (Narayanan and Selvakumar, 2016).

The first attempt at CPU cooling dates back to the early years of modern computing. In the 1950 and 1960, the first electronic computers, such as the UNIVAC I and the IBM 701, were cooled using cooling systems based on fans and passive heat exchangers. However, with the advancement of technologies and the increasing computing power of CPUs, cooling challenges started to arise. The early commercially available consumer processors, such as the Intel 8086 launched in 1978, also required efficient cooling solutions to prevent overheating and ensure stable performance (Alssaraf et al., (2020).

Naphon and Wiriyasart (2009) investigated liquid cooling in a mini-rectangular fin heatsink with and without thermoelectricity for the central processing unit. Their results are expected to provide guidelines for designing a cooling system that enhances the heat transfer performance of electronic equipment. Tzou et al. (2010) examined the thermal conductivity of thin films deposited on aluminum alloy substrates using different sputtering methods. They concluded that sputtering method and power were the most significant factors among the five controllable factors affecting the thermal conductivity of the aluminum substrate in the sputtering process. Lau and Srinivasan (2016) proposed leveraging parallel GPU computing to enhance the computational efficiency of Sim-Opt. Xiahou et al. (2019) addressed and developed a vertical radiator with multiple-pulse condensation ends and a flat evaporation end for vertical cooling of the central processing unit (CPU). They demonstrated that when the radiator operates stably, the optimal filling rate is 25%. Zhao et al. (2019) established and validated a set of experiments to investigate the flow and heat transfer characteristics of nanofluids circulating in the central processing unit (CPU). They found that there is an optimal nanoparticle mass fraction and groove depth to achieve the lowest temperature of the CPU. Yang et al. (2018) studied heatsinks with integrated CPU heat pipes, finding a minimum thermal resistance. An H-shaped arrangement of integrated heat pipes showed the best performance, increasing cooling capacity by 22.5% and reducing weight by 30.1% compared to heatsinks without pipes. Siricharoenpanich et al. (2019) researched the thermal management system for CPU cooling using short heat pipes in a computer. They found that heat pipe tilt angles and working fluid properties had a significant impact on cooling capacity. Shahsavar et al. (2021) examined the effect of connection holes on a biologically synthesized silver/water nanofluid's performance in a microchannel heatsink. They showed that increasing nanofluid volume concentration and Reynolds number improve CPU temperature reduction. Wang et al. (2022) conducted numerical comparisons of forced convection in three different 3D heatsink configurations. Their results showed that heatsinks with metal foam had superior cooling performance. Shahsavar et al. (2022) studied the impact of nanoparticle shapes on flow and heat transfer in a helical microchannel heatsink for electronic cooling. The use of nanofluids showed significant improvement in heat transfer while resulting in increased pumping power.

In the context of cooling electronic materials through forced convection, improved geometric configurations have been developed. Rossi di Schio et al. (2022) numerically studied fluid flow and heat transfer of a nanofluid in a Couette flow configuration using the Buongiorno model. This configuration can be applied to electronic cooling operations. They found that the Nusselt number on the upper wall increased with the Reynolds number in most cases. Mokhefi and Rossi di Schio (2022) numerically investigated the impact of a magnetic field on forced convection of a nanofluid in a channel with an integrated cavity using the Buongiorno model. They found that the Nusselt number was positively influenced by the magnetic field inclination angle with a rate of 40%.

In the context of CPU cooling by natural convection in finned blocks equipped with heat pipes, Alssaraf et al. (2020) numerically studied heat transfer in a thermal dissipator using nanofluid under a uniform magnetic field. They optimized tube geometry allowing to intensify and improve the heat transfer rate. Anouar and Mokhefi (2022) numerically studied a CPU heatsink with a zigzagged wall filled with a nanofluid using Buongiorno two-phase flow model. They found that zigzag fins enhance cooling rates by about 4% compared to the standard configuration.

Based on the literature review of previous studies on CPU cooling using various methods, it is evident that this field is of significant importance and has attracted considerable research attention. Active cooling using heatsinks filled with nanofluids and equipped with heat pipes has received particular interest in recent years. However, there are still gaps to explore in this type of cooling system. Therefore, the aim of this research is to contribute to the study of thermal and entropy behavior within the natural electronic heatsink equipped with four pipes to improve cooling performance in presence of a hybrid nanofluid. The effects of several parameters, such as buoyancy, magnetic field, its angle and nanoparticles have been highlighted on cooling capacity. Additionally, the radial disposition of tubes has been examined to optimize the best position in terms of thermal transfer and irreversibility to enhance the design procedure of such heatsinks.

2. Problem description

The geometry of the heatsink presented in this study is characterized by a parallelepiped-shaped block of length *Lo*, width *l*, and height *H*, designed to ensure optimal heat transfer. This block is crossed by four cylindrical tubes of diameter *D*, also known as heat pipes, which play an important role in the cooling process (Fig. 1). These heat pipes, acting as efficient thermal conductors, function to transport the heat generated by the CPU inside the heatsink. They serve as transfer channels, efficiently allowing the heat to flow from the point of generation to the cooling fluid, which, in the present case, is a hybrid nanofluid, (Fig. 1).

The nanofluid, filled inside the block, is specifically formulated for its excellent thermal properties and plays an important role in absorbing and dissipating the heat generated by the CPU. With the help of the heat pipes, the heat is transferred from the CPU to the nanofluid, which acts as a thermal reservoir. Subsequently, the heat is naturally dissipated into the nanofluid through the effect of the fins arranged on the boundaries of the block. These fins, designed to maximize the thermal exchange surface, facilitate heat dissipation into the surrounding environment, thereby maintaining the CPU at an optimal operating temperature. It is important to emphasize that the heatsink presented in this paper belongs to the category of active cooling methods. Furthermore, it is important to highlight that the utilized nanofluid is also subjected to the buoyancy effect. Buoyancy refers to the fluid's tendency to move based on density differences induced by temperature variations. When the nanofluid is heated by the CPU-generated heat, its density may change, resulting in convection and circulation movements within the heatsink.

These convection movements can significantly influence the heat distribution and thermal transfer within the system.

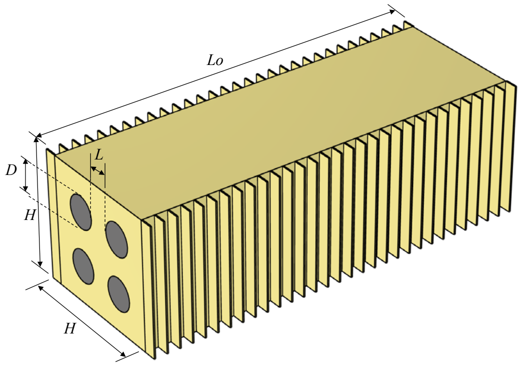

Fig. 1. Cooling block of an active CPU heatsink.

In this study, the complexity of the heatsink geometry is simplified to adhere to a two-dimensional model. The adopted configuration takes the form of a square, representing the domain of the heatsink. Inside this square, there are four circles, symbolizing the cylindrical tubes of the heatsink numbered from 1 to 4, (Fig. 2). In this simplified model, the four circular regions of the heatsink are maintained at a constant hot temperature Th, representing the heat generated by the CPU. In contrast, the right and left boundaries of the square are maintained at a cold temperature Tc, simulating the cooling effect produced by the heatsink fins in a real configuration. This setup also enables the dissipation of heat from the nanofluid and maintains a favorable thermal gradient. The upper and lower walls of the square are considered adiabatic, meaning that there is no heat transfer across these boundaries ($q = 0$). In this simplified situation, the objective is to evaluate the efficiency of thermal transfer between the nanofluid and the heatsink tubes. The study focuses on analyzing temperature variations and thermal gradients throughout the nanofluid, based on the imposed temperatures and nanofluid characteristics.

The heatsink block is filled with a hybrid nanofluid, combining two types of nanoparticles, namely Al_2O_3 (alumina) and CuO (copper oxide), with H_2O (pure water) as the base. This combination of elements imparts improved thermal and heat transfer properties to the nanofluid compared to pure water. Indeed, the combination of Al_2O_3 and CuO as hybrid nanoparticles in the nanofluid imparts synergistic properties that optimize thermal transfer performance. The thermo-physical properties of all the mentioned substances, namely pure water, Al_2O_3, and CuO, are listed in Table 1.

Material	**Water (f)**	**Al_2O_3 (p)**	**CuO (p)**
Density [kg/m^3]	997.1	3970	6500
Thermal capacity [J/(kg. K)]	4179	765.0	540.0
Thermal conductivity [W/(m.K)]	0.613	40.00	18.00
Dynamic viscosity [kg/(m.s)]	0.001	--	--
Thermal expansion [10^{-5}.1/K]	21.00	0.850	0.8500
Electric conductivity [S/m]	0.050	1×10^{-12}	2.7×10^{-8}

Table 1. The thermo-physical properties of the nanofluid.

In this study, the effect of magnetic field B according to different inclination angles γ on the flow of hybrid nanofluid inside the heatsink block has been introduced Fig. 2).

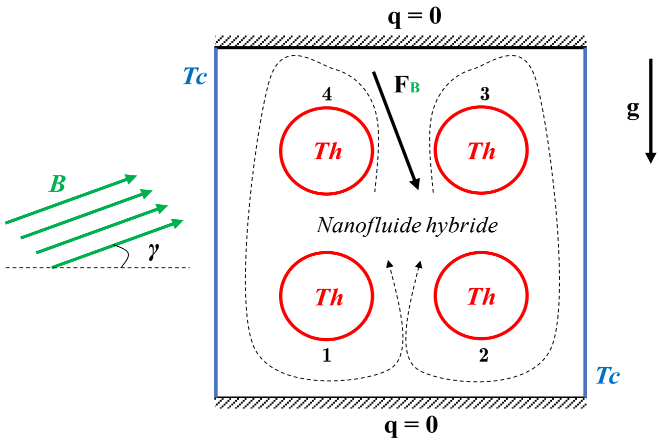

Fig. 2. 2D Reduced geometry of the CPU heatsink.

In this study, the hybrid nanofluid (Ranga et al., 2019) composed of alumina nanoparticles (Al_2O_3) and copper oxide nanoparticles (CuO) circulates inside a CPU heatsink system, as illustrated in Fig. 2. The percentage of both types of oxide-metal nanoparticles in the suspension in pure water is equal (50%-50%). Furthermore, in order to compare the thermal and entropic performances of this hybrid nanofluid type, it has been deemed necessary in this study to examine nanofluids with Al_2O_3 and CuO nanoparticles suspended independently in pure water, as well as pure water as a reference case. Let φ represent the volume fraction of hybrid nanoparticles suspended in pure water. If we consider Vo as the volume of different substances, p denotes the nanoparticles, and f denotes the base fluid (pure water), it is possible to calculate the volume fraction of nanoparticles as given by (Ranga et al., 2019):

$$\varphi = \frac{Vo_{\mathrm{p}}}{Vo_{\mathrm{p}} + Vo_{\mathrm{f}}} = \varphi_{\mathrm{Al_2O_3}} + \varphi_{\mathrm{CuO}} \tag{1}$$

$$\varphi_{\mathrm{Al_2O_3}} = \frac{Vo_{\mathrm{Al_2O_3}}}{Vo_{\mathrm{p}} + Vo_{\mathrm{f}}} \text{ and } \varphi_{\mathrm{CuO}} = \frac{Vo_{\mathrm{CuO}}}{Vo_{\mathrm{p}} + Vo_{\mathrm{f}}} \tag{2}$$

According to the laws of standard and nanometric suspensions, the different thermo-physical properties of the hybrid nanofluid depend on both the overall volume fraction and the specific volume fraction of each type of oxide-metal nanoparticles. Based on the overall volume fraction of nanoparticles, the effective density (ρ_{nf}), dynamic viscosity (μ_{nf}), thermal conductivity (k_{nf}), specific heat capacity (Cp_{nf}), thermal expansion coefficient (βnf), and electrical conductivity (σ_{nf}) of the hybrid nanofluid are respectively given by the following equations (Maxwell, 1881; Brinkman, 1952):

$$\rho_{\mathrm{nf}} = \varphi \rho_{\mathrm{p}} + (1-\varphi)\rho_{\mathrm{f}} \tag{3}$$

$$\mu_{\mathrm{nf}} = \mu_{\mathrm{f}} (1-\varphi)^{-2.5} \tag{4}$$

$$\frac{k_{\text{nf}}}{k_{\text{f}}}=\frac{k_{\text{p}}+2k_{\text{f}}-2\varphi(k_{\text{f}}-k_{\text{p}})}{k_{\text{p}}+2k_{\text{f}}+\varphi(k_{\text{f}}-k_{\text{p}})} \tag{5}$$

$$(\rho Cp)_{\text{nf}}=\varphi(\rho Cp)_{\text{p}}+(1-\varphi)(\rho Cp)_{\text{f}} \tag{6}$$

$$(\rho\beta)_{\text{nf}}=\varphi(\rho\beta)_{\text{p}}+(1-\varphi)(\rho\beta)_{\text{f}} \tag{7}$$

$$\sigma_{\text{nf}}=\varphi\sigma_{\text{p}}+(1-\varphi)\sigma_{\text{f}} \tag{8}$$

The thermo-physical properties of the hybrid nanoparticles of Al_2O_3 and CuO are calculated based on each specific fraction as follows (Moghadasi et al., 2020):

$$\varphi\rho_{\text{p}}=\varphi_{\text{Al}_2\text{O}_3}\rho_{\text{Al}_2\text{O}_3}+\varphi_{\text{CuO}}\rho_{\text{CuO}} \tag{9}$$

$$\varphi\mu_{\text{p}}=\varphi_{\text{Al}_2\text{O}_3}\mu_{\text{Al}_2\text{O}_3}+\varphi_{\text{CuO}}\mu_{\text{CuO}} \tag{10}$$

$$\varphi k_{\text{p}}=\varphi_{\text{Al}_2\text{O}_3}k_{\text{Al}_2\text{O}_3}+\varphi_{\text{CuO}}k_{\text{CuO}} \tag{11}$$

$$\varphi Cp_{\text{p}}=\varphi_{\text{Al}_2\text{O}_3}Cp_{\text{Al}_2\text{O}_3}+\varphi_{\text{CuO}}Cp_{\text{CuO}} \tag{12}$$

$$\varphi\beta_{\text{p}}=\varphi_{\text{Al}_2\text{O}_3}\beta_{\text{Al}_2\text{O}_3}+\varphi_{\text{CuO}}\beta_{\text{CuO}} \tag{13}$$

$$\varphi\sigma_{\text{p}}=\varphi_{\text{Al}_2\text{O}_3}\sigma_{\text{Al}_2\text{O}_3}+\varphi_{\text{CuO}}\sigma_{\text{CuO}} \tag{14}$$

3. Governing equations

3.1 Governing dimensional equations

In this subsection, the presentation focuses on the dimensional description of the equations governing the cooling studied phenomenon. Using the principles of conservation of mass, momentum and energy, a system of equations can be established that accurately represents various forces and flows involved. The dimensional equations are based on real physical dependent variables such as fluid velocity (v), pressure (p) and temperature (T). These variables are associated with the various thermo-physical properties of the hybrid nanofluid used, as well as with the geometry of the heatsink. As this is a two-dimensional, stationary study for an incompressible nanofluid following in a laminar regime, the above balances by developing their equations in a Cartesian reference frame only along the x and y abscissa directions can be expressed. Hence, the velocity field acquires two components along these directions $\mathbf{v} = (u, v)$. In addition, the magnetic field is defined by $\mathbf{B} = (B_x, B_y)$. Given that: $B_x = B\cos\gamma$ and $B_y = B\sin\gamma$ and that the pressure p is defined by its hydrostatic value, the final system will be:

$$\frac{\partial u}{\partial x}+\frac{\partial v}{\partial y}=0 \tag{15}$$

$$\rho_{nf}\left(u\frac{\partial u}{\partial x}+v\frac{\partial u}{\partial y}\right)=-\frac{\partial p}{\partial x}+\mu_{nf}\left(\frac{\partial^2 u}{\partial x^2}+\frac{\partial^2 u}{\partial y^2}\right)+\sigma B^2(v\cos\gamma\sin\gamma-u\sin^2\gamma) \tag{16}$$

$$\rho_{nf}\left(u\frac{\partial v}{\partial x}+v\frac{\partial v}{\partial y}\right)=-\frac{\partial p}{\partial y}+\mu_{nf}\left(\frac{\partial^2 v}{\partial x^2}+\frac{\partial^2 v}{\partial y^2}\right)+\sigma B^2(u\sin\gamma\cos\gamma-v\cos^2\gamma)+\rho_{nf}g\beta_{nf}\left(T-T_c\right) \tag{17}$$

$$\rho_{nf}Cp_{nf}\left(u\frac{\partial T}{\partial x}+v\frac{\partial T}{\partial y}\right)=k_{nf}\left(\frac{\partial^2 T}{\partial x^2}+\frac{\partial^2 T}{\partial y^2}\right) \tag{18}$$

3.2 Governing dimensionless equations

The dimensionless mathematical transformation simplifies the governing equations by eliminating dimensional variables and expressing them as unitless numbers. This facilitates the analysis and numerical resolution of the equations, while preserving the essential physical properties of the system under study. Hence, dimensionless variables obtained by dividing the dimensional variables by reference variables have been defined as follows:

$$\left(U,V\right)=\frac{H\left(u,v\right)}{\alpha_{\mathrm{nf}}},\ P=\frac{H^2 p}{\rho\alpha_{\mathrm{nf}}{}^2},\Theta=\frac{T-T_c}{T_h-T_c},\left(X,Y\right)=\frac{\left(x,y\right)}{H} \tag{19}$$

By substituting these dimensionless Eq. (19) variables into the dimensional governing equations Eqs. (15)-(18), the dimensionless governing equations are:

$$\frac{\partial U}{\partial X}+\frac{\partial V}{\partial Y}=0 \tag{20}$$

$$U\frac{\partial U}{\partial X}+V\frac{\partial U}{\partial Y}=-\frac{\partial P}{\partial X}+\frac{k_{\mathrm{f}}}{k_{\mathrm{nf}}}\frac{(\mu Cp)_{\mathrm{nf}}}{(\mu Cp)_{\mathrm{f}}}\mathrm{Pr}\left(\frac{\partial^2 U}{\partial U^2}+\frac{\partial^2 V}{\partial Y^2}\right)+\frac{\sigma_{nf}}{\sigma_f}\frac{k_{\mathrm{f}}}{k_{\mathrm{nf}}}\frac{Cp_{\mathrm{nf}}}{Cp_{\mathrm{f}}}\mathrm{Ha}^2\mathrm{Pr}(V\sin\gamma\cos\gamma-V\sin^2\gamma) \tag{21}$$

$$U\frac{\partial V}{\partial X}+V\frac{\partial V}{\partial Y}=-\frac{\partial P}{\partial Y}+\frac{k_{\mathrm{f}}}{k_{\mathrm{nf}}}\frac{(\mu Cp)_{\mathrm{nf}}}{(\mu Cp)_{\mathrm{f}}}\mathrm{Pr}\left(\frac{\partial^2 V}{\partial X^2}+\frac{\partial^2 V}{\partial Y^2}\right)+\frac{\beta_{\mathrm{nf}}}{\beta_{\mathrm{f}}}\left(\frac{\alpha_{\mathrm{f}}}{\alpha_{\mathrm{nf}}}\right)^2\mathrm{Pr.Ra}\Theta+\frac{\sigma_{nf}}{\sigma_f}\frac{k_{\mathrm{f}}}{k_{\mathrm{nf}}}\frac{Cp_{\mathrm{nf}}}{Cp_{\mathrm{f}}}\mathrm{Ha}^2\mathrm{Pr}(U\sin\gamma\cos\gamma-V\cos^2\gamma) \tag{22}$$

$$U\frac{\partial\Theta}{\partial X}+V\frac{\partial\Theta}{\partial Y}=\frac{\partial^2\Theta}{\partial X^2}+\frac{\partial^2\Theta}{\partial Y^2} \tag{23}$$

The dimensionless stream function (Ψ) describing the flow streamlines and the mass flow is given by the following two equations:

$$\frac{\partial\Psi}{\partial X}=-V\ ,\ \frac{\partial\Psi}{\partial Y}=U \tag{24}$$

The dimensionless Poisson equation permits to resolve the above equations Eq. (24) from a unique equation of a second order:

$$\frac{\partial^2\Psi}{\partial X^2}+\frac{\partial^2\Psi}{\partial Y^2}=\frac{\partial U}{\partial Y}-\frac{\partial V}{\partial X} \tag{25}$$

In the context of the present study, the dimensionless equations reveal important dimensionless numbers that characterize the cooling phenomenon. These include the Prandtl number (Pr), the Rayleigh number (Ra) and the Hartmann number (Ha). They are given by:

$$\mathrm{Pr}=\frac{\mu_f Cp_f}{k_f},\ \mathrm{Ra}=\frac{g\beta_f\left(T_h-T_c\right)H^3}{\alpha_f \nu_f},\ \mathrm{Ha}=HB\sqrt{\frac{\sigma_f}{\mu_f}} \tag{26}$$

Note that α and υ present the thermal diffusivity and kinematic viscosity, respectively, which are given by:

$$\alpha=\frac{k}{\rho Cp},\nu=\frac{\mu}{\rho} \tag{27}$$

3.3 Boundary conditions

In the present dimensionless approach, it is also needed to formulate boundary conditions in a dimensionless way accompanied with the governing system Eqs. (20)-(23). These conditions describe the values or behaviors of variables at the boundary of the study domain. By dimensioning these boundary conditions, it is ensured that they are consistent with the dimensionless equations. These boundary conditions are:

Tube walls: considered hot at Th temperature:

$$u=v=0\Rightarrow U=V=0\,,T=T_h\Rightarrow\Theta=1 \tag{28}$$

Left and right-side walls: considered cold at temperature Tc:

$$u=v=0\Rightarrow U=V=0\,,T=T_c\Rightarrow\Theta=0 \tag{29}$$

Upper and lower horizontal walls: considered adiabatic (thermally insulated):

$$u=v=0\Rightarrow U=V=0\,,\frac{\partial T}{\partial y}=0\Rightarrow\frac{\partial\Theta}{\partial y}=0 \tag{30}$$

3.4 Heat transfer rate

Heat transfer rate, also known as thermal transfer rate, is a measure of the amount of heat transferred per unit of time between a system and its environment. It represents the rate at which heat is exchanged or dissipated. In the context of cooling CPUs with nanofluids, the heat transfer rate is of paramount importance. It measures the efficiency of the cooling process in terms of dissipating the heat generated by the processor. The Nusselt number is a dimensionless characteristic that relates the convective heat transfer rate to the fluid properties and geometric characteristics of the system. The general formula for calculating the Nusselt number (Nu) depends on the type of flow and the specific configuration of the system. In CFD, it is calculated locally at any position by:

$$\mathrm{Nu}_l=\frac{k_{nf}}{k_f}\left(\frac{hH}{k_f}\right)=\frac{k_{nf}}{k_f}\frac{H}{T_h-T_c}\frac{\partial T}{\partial n} \tag{31}$$

By dimensioning the physical quantities, it is obtained:

$$\mathrm{Nu}_l=\frac{k_{nf}}{k_f}\frac{\partial\Theta}{\partial N} \tag{32}$$

In the present study, the Nusselt number is calculated on the circumferences of cooling tubes maintained at a hot temperature. The average Nusselt number, in this study, represents the average of the local Nusselt numbers of the four cooling tubes considered simultaneously. It is calculated by adding the average Nusselt number of each tube and dividing the total by the number of tubes. The average Nusselt number of a single tube of order i with i = 1,2,3 and 4 is given by:

$$\mathrm{Nu}_i = \frac{H}{\pi D}\frac{k_{nf}}{k_f}\int_{\mathrm{Tubei}} \frac{\partial \Theta}{\partial N}\mathrm{d}\ell \tag{33}$$

Consequently, the average of this number for the four tubes is given by:

$$\mathrm{Nu} = \frac{1}{4}\sum_{i=1}^{4}\frac{H}{\pi D}\frac{k_{nf}}{k_f}\int_{\mathrm{Tubei}} \frac{\partial \Theta}{\partial N}\mathrm{d}\ell \tag{34}$$

3.5 Entropy generation

In this study, the entropy generation in the cooling system, which consists of a heatsink with four tubes immersed in a nanofluid inside a block is considered. Entropy is generated (Sgen) in this system mainly due to two factors: thermal generation (SHT) and fluid friction (SFF). Thermal generation of entropy is due to the conversion of thermal energy from the processor into energy dissipated in the cooling fluid. This conversion leads to an increase in system entropy. Fluid friction also contributes to entropy generation. As the fluid flows inside the nanofluid block, it encounters resistance due to friction against the tube walls and flow turbulence. The dimensionless generated entropy is given by:

$$S_{gen} = S_{HT} + S_{FF} \tag{35}$$

On the other hand, the entropy due to heat transfer is:

$$S_{HT} = \left(\frac{\partial \Theta}{\partial X}\right)^2 + \left(\frac{\partial \Theta}{\partial Y}\right)^2 \tag{36}$$

The dimensionless generated global entropy is:

$$S_{FF} = \chi\left[2\left(\frac{\partial U}{\partial X}\right)^2 + 2\left(\frac{\partial V}{\partial Y}\right)^2 + \left(\frac{\partial U}{\partial Y} + \frac{\partial V}{\partial X}\right)^2\right] \tag{37}$$

The dimensionless generated global entropy is:

$$S_{gen} = \left(\frac{\partial \Theta}{\partial X}\right)^2 + \left(\frac{\partial \Theta}{\partial Y}\right)^2 + \chi\left[2\left(\frac{\partial U}{\partial X}\right)^2 + 2\left(\frac{\partial V}{\partial Y}\right)^2 + \left(\frac{\partial U}{\partial Y} + \frac{\partial V}{\partial X}\right)^2\right] \tag{38}$$

The coefficient χ is a dimensionless parameter characterizing the fluid, its expression:

$$\chi = \frac{\mu_{nf}\alpha_{nf}^2 T_0}{k_{nf} H\left(T_h - T_c\right)^2} \tag{39}$$

The Bejan number is a dimensionless number used to characterize the coupling between heat and mass transfer phenomena. It is widely used in the study of thermal systems and their performance in terms of energy efficiency. The Bejan number (Be) is defined as the ratio between the entropy generated due to heat transfer (SHT) and the average entropy generated (Sgen) in a given system. The averaged Bejan number is calculated by:

$$\overline{\mathrm{Be}} = \frac{\overline{s_{HT}}}{\overline{s_{HT} + s_{FF}}} = \frac{\overline{S_{HT}}}{\overline{S_{HT} + S_{FF}}} \tag{40}$$

4. Numerical method

4.1 Numerical procedures

In the numerical solution part, the Galerkin finite element method to solve the Navier-Stokes and heat equations has been used (Taylor and Hood, 1973). This method is widely used for the numerical solution of partial differential equations. The finite element method is based on the discretization of the simulation domain into a set of finite elements. Each finite element is defined by nodes, and the unknowns of the problem are approximated by interpolation functions on these elements. In our study, we used a non-linear approximation on the elements to take into account the non-linear effects of the cooling phenomenon (Dechaumphai, 1999). Once the domain is discretized into finite elements, the Navier-Stokes and heat equations are transformed into a system of linear equations. To solve this system, we used the iterative Gauss-Seidel method. This method progressively solves the equations by iteratively updating the unknowns until satisfactory convergence is achieved. Using the Galerkin finite element method and the iterative Gauss-Seidel method implemented in COMSOL Multiphysics 6.0 software, we were able to obtain accurate numerical solutions for the Navier-Stokes and heat equations in the present simulation domain. These solutions were obtained by taking into account the boundary conditions, the physical properties of the fluid and material, and the specific configurations of our study.

4.2 Mesh

In the present investigation, a structured triangular mesh to represent the simulation domain has been used. This type of mesh is characterized by regular triangular elements covering the entire domain.

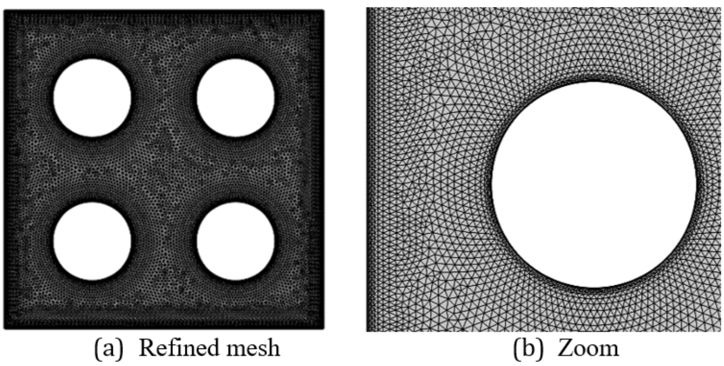

Fig. 3. Refined mesh of the study domain with zoom.

It offers good regularity and facilitates numerical calculation. To accurately capture phenomena, close to the tube and block walls, it has been also added a rectangular boundary layer grid in the areas close to these walls. This boundary layer grid is made up of rectangular cells aligned along the wall surfaces(Fig. 3). It enables fine resolution of convection and heat transfer phenomena occurring near walls, where temperature and velocity gradients are high. Using this combination of structured triangular mesh and rectangular boundary layer grid, we were able to achieve precise resolution of the cooling phenomenon in our simulation domain.

4.3 Mesh test

In order to obtain computation consistency, the reliability of the mesh used for numerical simulation has been examined. Hence, variations in the number of mesh elements and observed the evolution of various system characteristics as a function of these changes have been carried out. More specifically, variations in temperature, stream function, Nusselt number and Bejan number have been studied. It started with a reference value for the mesh, gradually increasing the number of elements to obtain finer meshes. At each stage, the results were recorded and compared with those obtained with the reference mesh.

Elements	9482	15512	22204	30280	39034
Time	8 s	12 s	18 s	26 s	34 s
T_{ave}	0.70863	0.70865	0.70865	0.70865	0.70865
Nu	4.12170	4.12344	4.12437	4.12505	4.12554
$(S_{gen})_{ave}$	29.5151	29.5280	29.5356	29.5422	29.5490
Be	0.54569	0.54575	0.54578	0.54577	0.54577

Table 2. Evolution of various characteristics as a function of mesh.

Above a certain number of elements, i.e. 30280 (Table 2), all the results obtained were mesh independent. This means that the system characteristics such as temperature, stream function, Nusselt number and Bejan number converged to stable values and no longer varied significantly with finer mesh sizes. This observation of convergence enabled us to validate the reliability of the mesh used in the present simulations. Therefore, the results obtained from this mesh as representative can be considered. Moreover, a relative error of ε = 10-6 as a stopping criterion for the calculations has been adopted. This means an upper limit for the error between the results obtained at each iteration of the numerical resolution process and the expected results has been set.:

$$err = \left| \frac{\Phi^{n+1} - \Phi^{n}}{\Phi^{n+1}} \right| \prec \varepsilon \tag{41}$$

Once the error between successive iterations Φn and Φn+1 was less than 10-6, the solution obtained to be sufficiently accurate and stopped the calculation process has been considered. It should be noted that in this study, the calculation has been carried out using a microcomputer ASUS with 12 GB RAM, and an Intel(R) Core (TM) i7-8550U processor with a base frequency of 1.80 GHz, which can be increased to 4 GHz if required. Total simulation time for optimal meshing was 26 seconds. This information on hardware and calculation times provides an insight into the performance of the configuration used to run the simulations.

4.4 Code validation

In order to strengthen the credibility of our numerical results, we felt it necessary to carry out a validation by comparing the present results obtained using the calculation code with those already present in the literature, which relate to the present CPU cooling topic. Therefore, we referred to the work of Alsarraf et al. [26], who addressed similar issues. The numerical conditions of their study to ensure a consistent comparison have reproduced. In the comparative analysis, temperature profiles at a Rayleigh number (Ra) equal to 10^6, as well as entropy results at an Ra of 10^4 have been presented. In addition, to further strengthen the numerical results, the Nusselt number as function of the Rayleigh number for different configurations has been plotted. More specifically, the Nusselt number values on the left and right walls of the heatsink for a single nanofluid with a concentration of 0.03 alumina nanoparticles have been shown.

The thermal and entropy results obtained in this study showed a good agreement with those presented in the reference, as shown in Figs. 4 and 5. Moreover, the perfect superposition of the Nusselt number curves, illustrated in Fig. 6, further strengthens this agreement. These findings lead us to conclude that the present numerical results show a satisfactory agreement, confirming the relevance and reliability of the contribution in the field of CPU cooling.

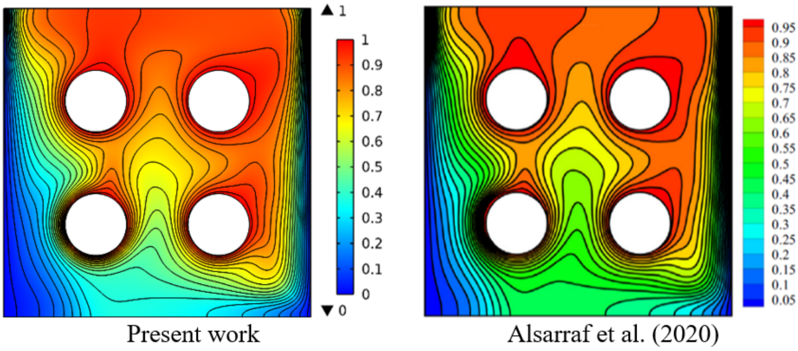

Fig. 4. Comparison of the thermal profile between the present work and that of Alsarraf et al. for Ra = 10^{-6}.

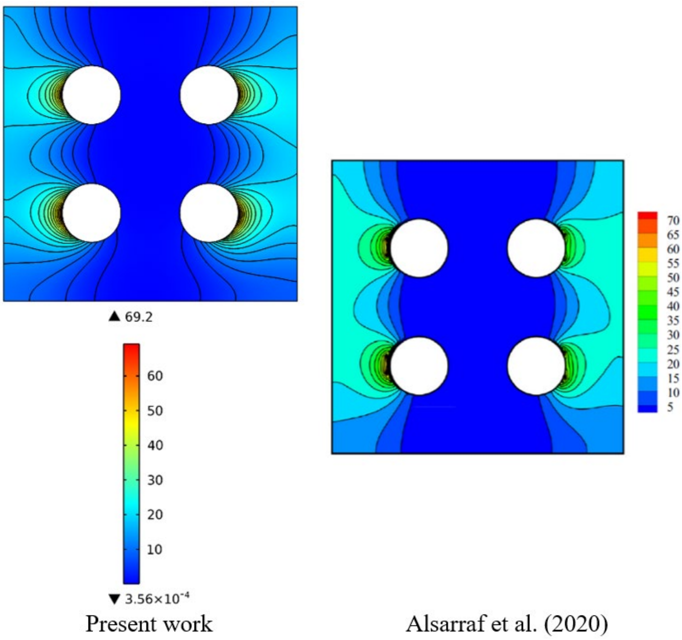

Fig. 5. Comparison of the entropy profile between the present work and that of Alsarraf et al. for Ra = 10^4.

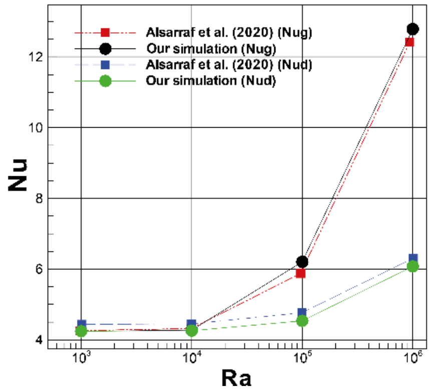

Fig. 6. Comparison of the Nusselt number between the present work and that of Alsarraf et al.

5. Results and discussion

In this section, the results of the numerical simulation of the laminar natural cooling phenomenon inside the CPU heatsink in the presence of a hybrid nanofluid containing alumina and copper oxide nanoparticles are presented. The effects of CPU-generated temperature ($10^3 < Ra < 10^6$), the magnetic field from neighboring electronic components ($0 < Ha < 100$), nanoparticle hybridization ($10^3 < \varphi < 10^6$), and the radial disposition of cylindrical tubes ($0.1 < L/H < 0.4$) have been highlighted regarding thermal reliability and irreversibility within the heatsink. It is worth noting that the Prandtl number and the inclination angle of the magnetic field have been fixed at $Pr = 6.81$ and $\gamma = 0°$, respectively.

5.1 Influence of CPU temperature

To highlight the influence of CPU temperature, the Rayleigh number as an indicator has been used. Since the exact CPU temperature cannot be directly determined, a dimensionless approach to conduct the present study has been adopted. In this case, CPU temperature is one of the determining factors of the Rayleigh number, as it appears in the mathematical expression of this dimensionless parameter. By making the study dimensionless, we can compare the results obtained for different CPU temperatures in a consistent manner. This allows us to analyze the influence of temperature on cooling performance by observing variations in the Rayleigh number.

Figure 7 shows the velocity distribution of the hybrid nanofluid inside the cooling block, which is traversed by four tubes where the nanofluid flows naturally between them. We studied this velocity distribution for different values of the Rayleigh number, namely 103 to 106, which is a dimensionless parameter used to characterize the effect of buoyancy forces versus dissipative forces.

It has been observed that the flow velocity of the nanofluid increases progressively as the Rayleigh number increases due to density differences created in the nanofluid. These density differences generate buoyancy forces that lead to more intense circulation of the nanofluid. Specifically, a significant increase in nanofluid flow velocity near the left and right walls of the cooling block has been observed.

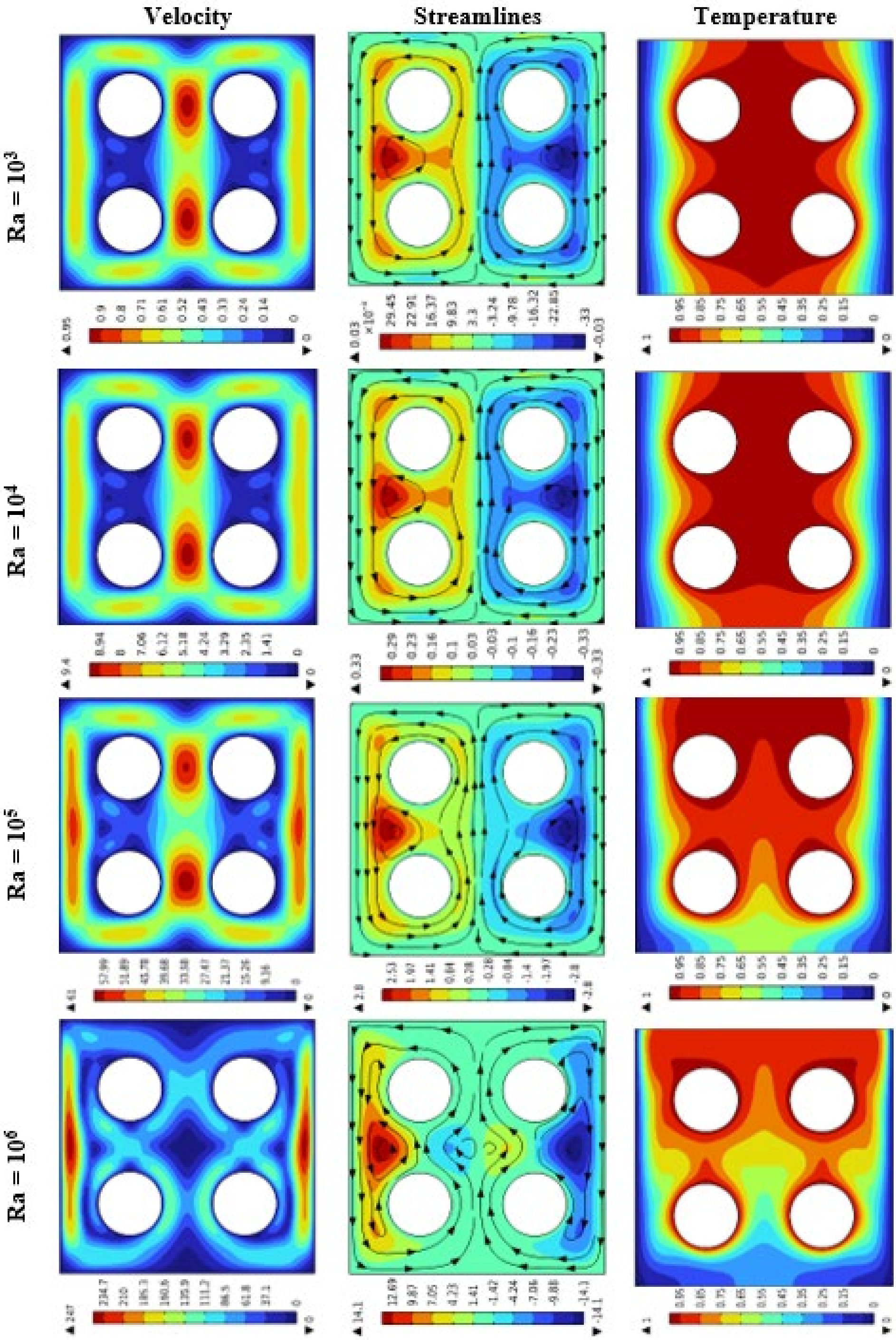

Fig. 7. Velocity contours, streamlines and temperature contours for different Rayleigh numbers at Pr = 6.8, Ha = 0, $\gamma = 0°$, $\varphi_1 = \varphi_2 = 0.02$ and $L/H = 0.2$.

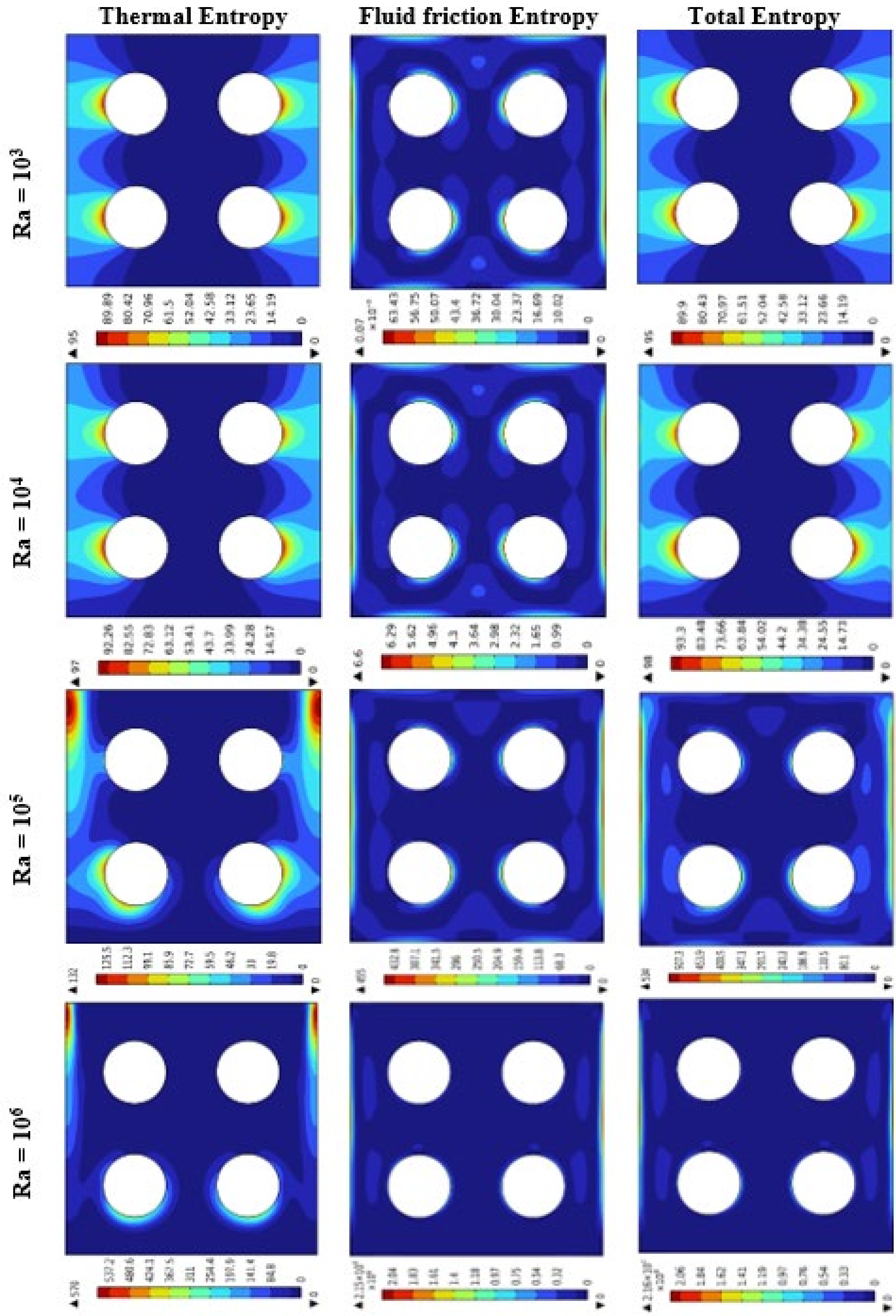

Fig. 8. Thermal, hydrodynamic and generated entropy contours for different Rayleigh numbers at Pr = 6.8, Ha = 0, $\gamma = 0°$, $\varphi_1 = \varphi_2 = 0.02$ and $L/H = 0.2$.

This is due to the interaction between buoyancy forces and the wall effect, which creates a flow acceleration. Moreover, this phenomenon leads to the formation of an additional vortex between the four tubes, promoting better nanofluid circulation. Hence, this indicates an increase in the system's heat transfer capacity, which is beneficial for CPU cooling. On the other hand, the effect of buoyancy encourages heat to rise to the top, resulting in improved cooling efficiency at the bottom of the block.

Figure 8 shows the evolution of entropy due to heat transfer and entropy due to nanofluid friction, as well as total entropy as a function of Rayleigh number. The entropy due to heat transfer reflects the disorder or irreversibility associated with heat transfer within the cooling block. It has been observed that this entropy increases with increasing Rayleigh number. This is due to the larger temperature gradients that are developed as heat transfer becomes more intense. These temperature gradients lead to increased heat fluxes, which in turn contribute to an increase in entropy due to heat transfer. As for the entropy due to nanofluid friction, it represents the irreversibility generated by resistance to fluid movement within the block and around the tubes. This entropy depends on the flow velocity of the nanofluid. An increase in the Rayleigh number leads to an increase in the flow velocity of the nanofluid, particularly in areas close to the block walls. As a result, the entropy due to fluid friction also increases with increasing Rayleigh number. Thus, total entropy exhibits an overall rise with the increasing Rayleigh number. On the over hand, at low Rayleigh numbers, thermal entropy predominates over that due to fluid friction. This means that the increase in entropy in the system is mainly due to heat transfer, i.e. temperature variations and heat exchange between the fluid and its environment. Moreover, as the Rayleigh number increases, the role of fluid friction becomes increasingly important.

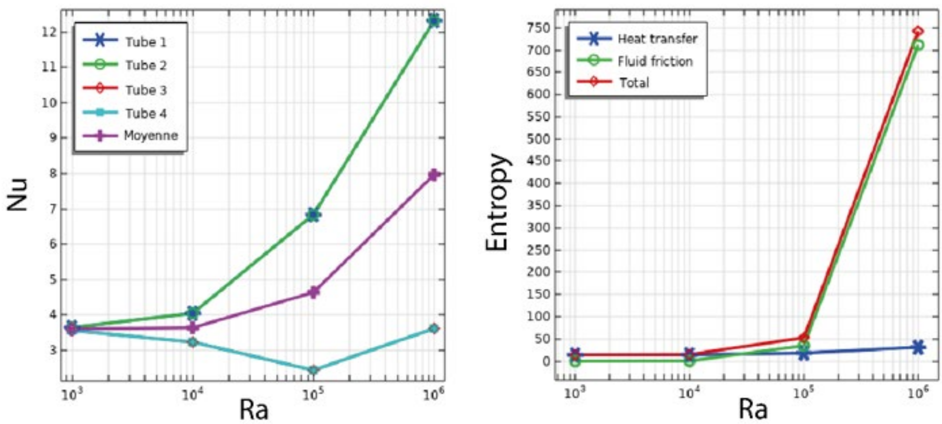

(a) Nusselt number (b) Entropy

Fig. 9. Variation of average Nusselt number for each tube and different average entropies for different Rayleigh numbers at Pr = 6.8, Ha = 0, $\gamma = 0°$, $\varphi_1 = \varphi_2 = 0.02$ and $L/H = 0.2$.

Figure 9 (a) shows the evolution of the Nusselt number for each tube as a function of the Rayleigh number. It is important to note that tubes numbered 1 and 2 are located in the lower part of the heatsink block, while tubes numbered 3 and 4 are in the upper part. It has been found that the Nusselt number of tubes 1 and 2 increases as the Rayleigh number increases. This means that heat transfer through these tubes is enhanced as the intensity of natural convection increases. On the other hand, the Nusselt number of tubes 3 and 4 at the top of the block decreases as the Rayleigh number increases, reaching a maximum value of around Ra = 10^5. Above this value, the Nusselt number for these tubes begins to rise again. This trend is attributed to changes in the velocity and temperature profiles of the fluid around the tubes as a function of the Rayleigh number. Indeed, under the action of buoyancy, the lower tubes are exposed to lower temperatures than the upper ones. This leads to improved cooling in the lower tubes compared with the upper tubes, which are influenced by the migration of hot fluid and its location in the upper part of the block. As the Rayleigh number increases, cooling capacity is reduced. As for the increase in the Nusselt number again with the Rayleigh number, this is due to the flow being favored and intensified by the buoyancy effect. Despite these specific variations, the mean value of the Nusselt numbers for the four tubes increases overall with the Rayleigh number. This indicates a general improvement in the convective heat transfer rate in the heatsink block as the intensity of natural convection increases. Figure 9 (b) shows the evolution of the average entropies generated by each process as a function of the Rayleigh number.

Ra	10^3	10^4	10^5	10^6
Nu	3.611	3.629	4.372	7.325
%Nu	--	0.498	21.07	102.8
Be	0.999	0.975	0.435	0.057

Table 3. Average Nusselt number and Bejan number for different Rayleigh numbers at Pr = 6.8, Ha = 0, $\gamma = 0°$, $\varphi 1 = \varphi 2 = 0.02$ and L/H = 0.2.

The average entropy due to heat transfer remains low and relatively constant for Rayleigh numbers below 10^5. However, above this Rayleigh number, the mean entropies due to fluid friction and the overall entropy increase abruptly, reaching significantly higher levels. This increase suggests that the fluid friction process becomes more dominant in entropy generation than heat transfer. This observation highlights the importance of fluid friction at high Rayleigh numbers in the thermodynamic behavior of the system.

In table 3, the Nusselt and Bejan number data as a function of Reynolds number have been presented. The percentage increase in Nusselt number between Ra = 10^3 and 10^4 is 0.49%, indicating a slight improvement in heat transfer at higher Reynolds numbers. However, the percentage increase between Ra = 10^3 and 10^6 reaches 102%, suggesting a significant increase in the rate of heat transfer. This greater increase in the Nusselt number as the Reynolds number increases is of particular importance for CPU cooling. On the other hand, when the Bejan number decreases as the Rayleigh number increases, this indicates that the irreversibility due to heat transfer become less significant in relation to the system as a whole. In other words, the cooling system becomes more efficient and shows better energy optimization. This can be attributed to improved heat transfer and reduced energy losses, resulting in fewer irreversibility.

5.2 Influence of leaky magnetic field

In this section, the impact of the leaked magnetic field on the behavior of the hybrid nanofluid and the operating efficiency of the heat sink has been explored. The Hartmann number is a dimensionless parameter used to highlight the influence of the magnetic field on heat transfer through the Lorentz force, in the context of magnetohydrodynamics (MHD). The study of the influence of the leaky magnetic field through the Hartmann number allows us to understand how the presence of a magnetic field can modify the thermal and hydrodynamic characteristics of the cooling system. In Fig. 10, the velocity contours and temperature for different Hartmann numbers, corresponding to a horizontal applicated magnetic fields have been shown. As the Hartmann number increases, a significant decrease in the flow velocity of the hybrid nanofluid around the heatsink tubes has been seen. This decrease in flow velocity is accompanied by a reduction in the maximum stream function.

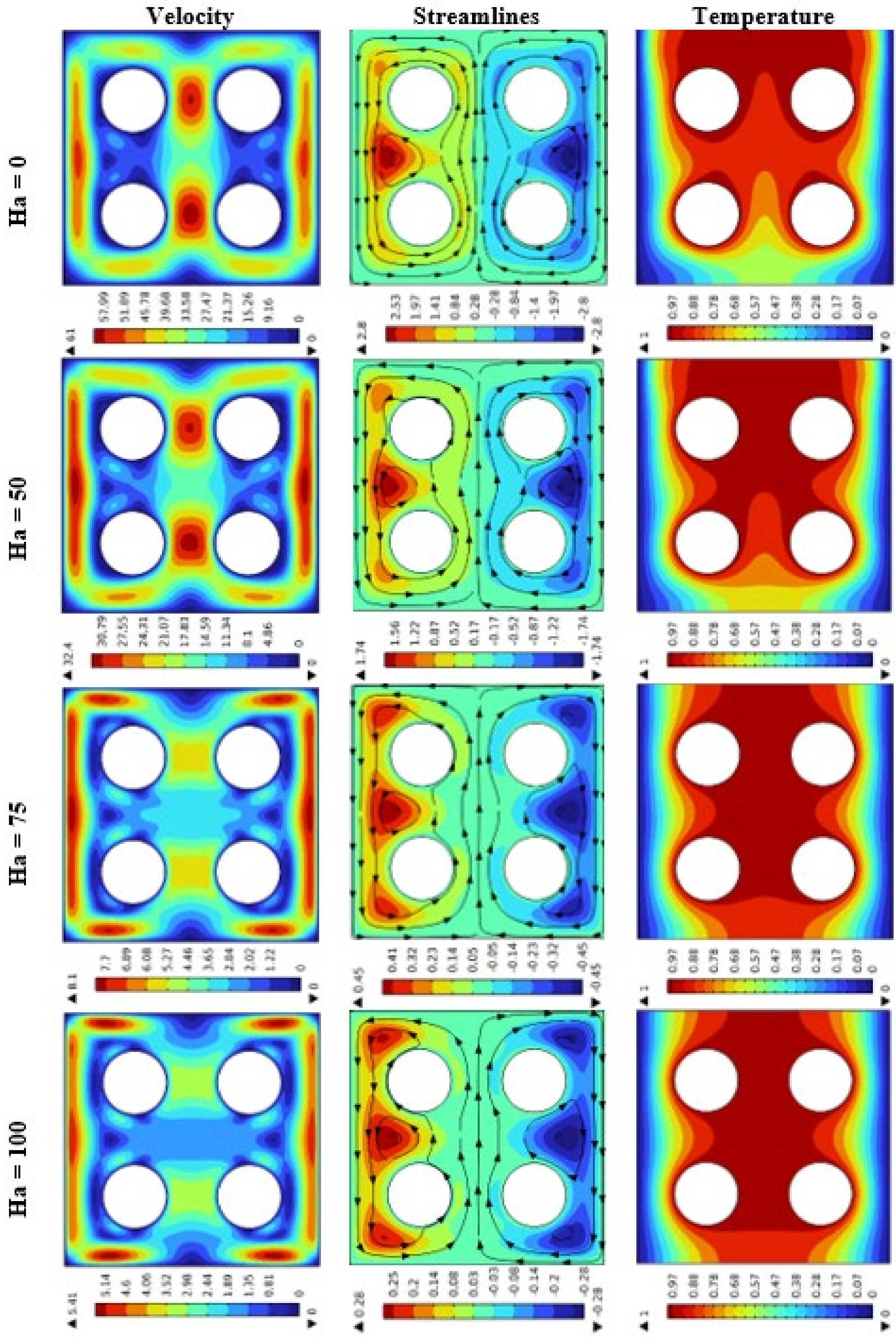

Fig. 10. Velocity contours, streamlines and temperature contours for different Hartmann numbers at Pr = 6.8, Ra = 10^5, $\gamma = 0°$, $\varphi_1 = \varphi_2 = 0.02$ and $L/H = 0.2$.

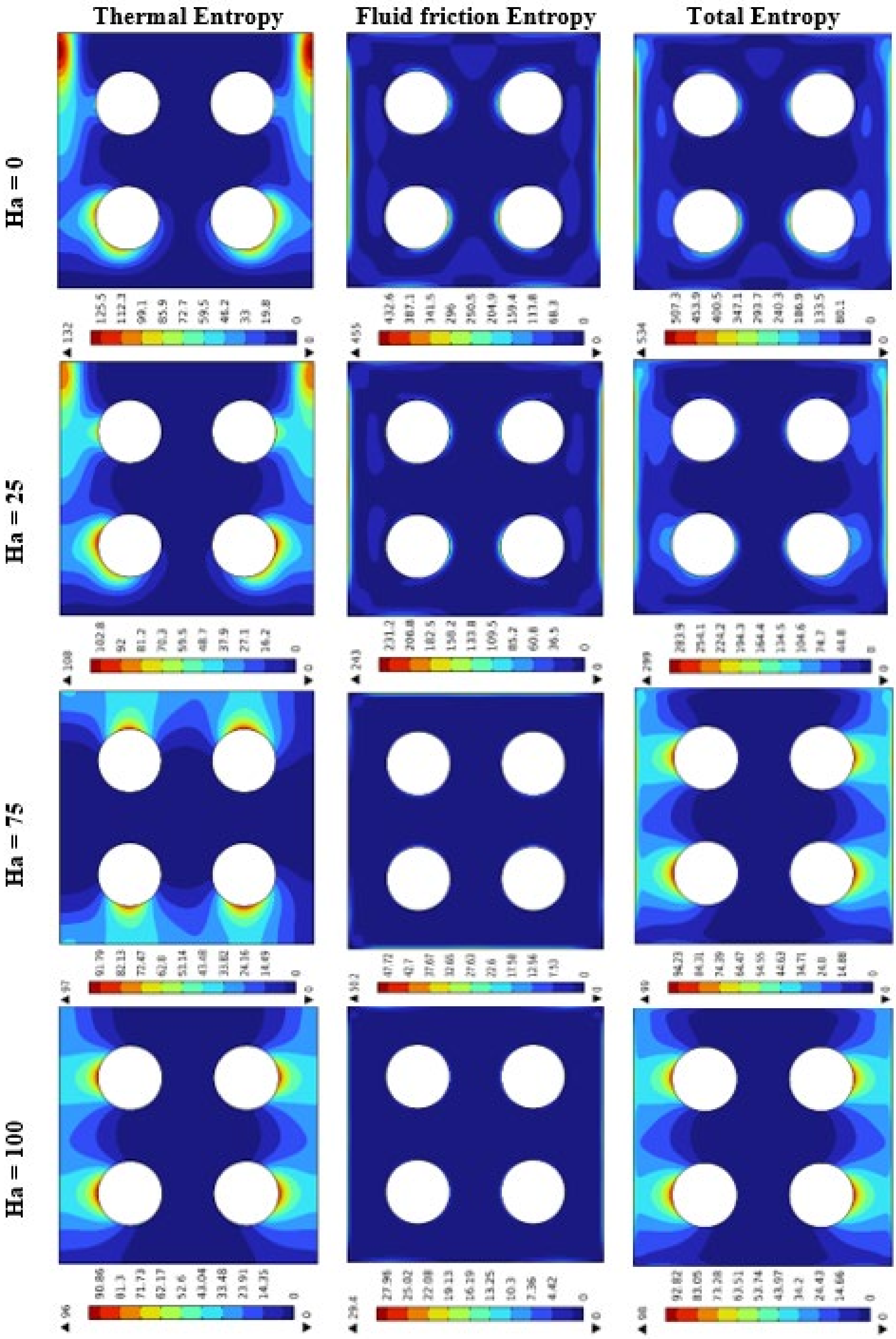

Fig. 11. Thermal, hydrodynamic and generated entropy contours for different Hartmann numbers at Ra = 10^5, Pr = 6.8, $\gamma = 0°$, $\varphi_1 = \varphi_2 = 0.02$ and $L/H = 0.2$.

In other words, the flow of the nanofluid is less intense, leading to a reduction in fluid flow around the heatsink tubes. This reduction in the stream function can be attributed to the influence of the magnetic field, which exerts a Lorentz force on the nanofluid, opposing its movement.

As a result, it has been found that the buoyancy effect is less dominant compared to the effect of the magnetic field at this angle. This reduced buoyancy effect can lead to a redistribution of heat within the cooling block, with greater heat accumulation inside the block slightly than around the tubes.

Figure 11 shows the evolution of entropy as a function of Hartmann number for different processes: thermal entropy, entropy due to fluid friction and total entropy. Contrary to what has been observed for the Rayleigh number, it has been found a decrease in entropy in all cases as the Hartmann number increases. Indeed, thermal entropy, which is related to heat transfer, decreases as the Hartmann number increases, becoming predominant. Consequently, total entropy also shows an overall decrease with increasing Hartmann number. This decrease indicates an improvement in overall heat transfer efficiency and a reduction in energy losses due to friction.

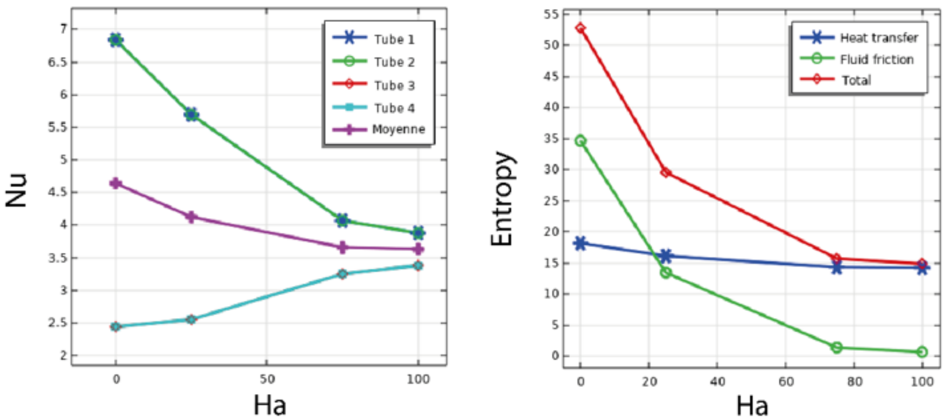

(a) Nusselt number (b) Entropy

Fig. 12. Variation of average Nusselt number for each tube and different average entropies for different Hartmann numbers at Pr = 6.8, Ra = 10^5, $\gamma = 0°$, $\varphi_1 = \varphi_2 = 0.02$ and $L/H = 0.2$.

Figure 12 (a) presents the Nusselt number for each tube as a function of the Hartmann number. different behaviors depending on the position of the tubes in the heat sink has been observed. For tubes located in the lower part of the heat sink, a decrease in the Nusselt number as the Hartmann number has been noted. The flow of the hybrid nanofluid around these tubes is reduced, which limits heat dissipation and leads to a decrease in the Nusselt number. On the other hand, for tubes located in the upper part of the heatsink, an increase in the Nusselt number as the Hartmann number has been noted. This is attributed to the interaction between the magnetic field and the hybrid nanofluid flow. Nevertheless, despite these specific variations in the tubes, a decrease in the average Nusselt number with increasing Hartmann number due to the predominance of its negative effect has been observed.

Figure 12 (b) shows the variation of the various mean entropies as a function of Hartmann number. A decrease in all mean entropies, particularly that due to nanofluid friction, has been observed. This indicates that the effect of the applicated magnetic field reduces entropy generation related to fluid friction. In addition, it has been found that, for high Hartmann values, entropy due to heat transfer becomes predominant over other entropies. This means that the effect of the magnetic field reduces the entropy due to heat transfer. Hence, the Bejan number is increased by the Hartmann number(Table 4).

Table 4 shows the influence of the magnetic field (Hartmann number) on CPU cooling capacity. It can be seen that the presence of the magnetic field can reduce cooling capacity by up to 21.75%. This percentage was obtained by comparing the case where Ha is equal to 100 with the case where Ha is equal to 0, i.e. in the absence of a magnetic field.

Ha	0	25	75	100
Nu	4.6423	4.1252	3.6617	3.6322
%Nu	--	-11.13	-21.12	-21.75
Be	0.3437	0.5456	0.9117	0.9550

Table 4. Average Nusselt number and Bejan number for different Hartmann numbers at Pr = 6.8, Ra = 10^5, $\gamma = 0°$, $\varphi_1 = \varphi_2 = 0.02$ and $L/H = 0.2$.

5.3 Influence of nanoparticle hybridization

Hybridization of CuO and Al2O3 nanoparticles suspended in pure water aims to exploit the specific advantages of each nanoparticle species in the cooling process. By combining these two types of nanoparticles, we hope to achieve a synergistic improvement in heat transfer properties and cooling capacity. The aim is to exploit the complementary characteristics of these nanoparticles to optimize the cooling efficiency of the hybrid fluid. In this study, the concentrations of the two species were set at equal parts (50%-50% of the total volume fraction) to assess the impact of this hybridization on cooling performance. The results obtained will enable us to determine whether this hybrid combination offers significant advantages over the use of each nanoparticle species individually.

Figures 13 to 15 show the effect of hybridizing Al2O3 and CuO nanoparticles by increasing the total volume fraction. Indeed, when hybridizing Al2O3 and CuO nanoparticles by increasing the total volume fraction, variations similar to those obtained when varying the volume fraction for each individual species has been noted. However, there are differences in the values of the various characteristics studied, such as velocity, stream function, Nusselt number and entropy generation. These differences can be explained by the specific properties of each nanoparticle species and their interaction in the hybrid fluid. On the other hand, increasing the volume fraction of nanoparticles leads to an increase in entropy due to heat transfer and a decrease in entropy due to fluid friction. When these two entropies intersect at the same value, they have a similar magnitude, reflected in a Bejan number of around 0.5.

The use of statistical histograms to compare the Nusselt numbers of different nanofluids based on alumina nanoparticles, CuO and a hybrid mixture at different concentrations enables to assess their heat transfer efficiency. It can be seen from figure 16 that alumina nanoparticles show the best heat transfer rate compared to CuO and hybrid nanoparticles. This improvement is explained by their specific properties. Alumina nanoparticles generally have better thermal conductivity than CuO, which facilitates heat transfer through the fluid. The superior thermal conductivity of alumina nanoparticles results in better heat dissipation and improved heat transfer rates. Although the percentage differences between the heat transfer rates of the different nanoparticle species are not significant, it is important to consider other criteria such as economic cost when selecting the optimum nanofluid (Table 5).

In this context, the suggestion to use alumina nanoparticles is justified by their relatively higher heat transfer efficiency compared to CuO and hybrid mix, as well as by probably wider commercial availability and potentially lower costs.

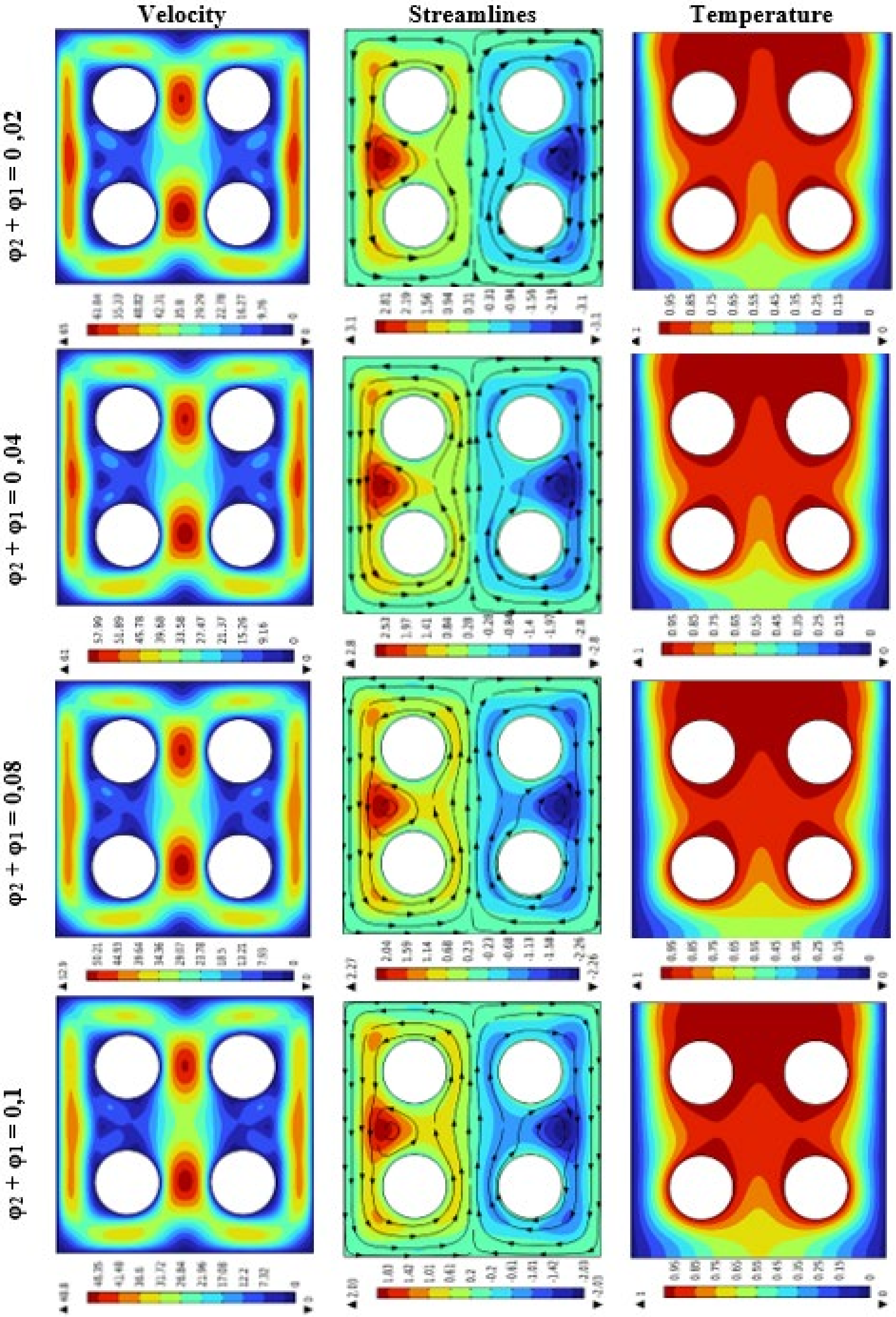

Fig. 13. Velocity contours, streamlines and temperature contours for different volume fractions of hybrid nanoparticles at Ra = 10^5, Pr = 6.8, Ha = 0, $\gamma = 0°$, and $L/H = 0$.

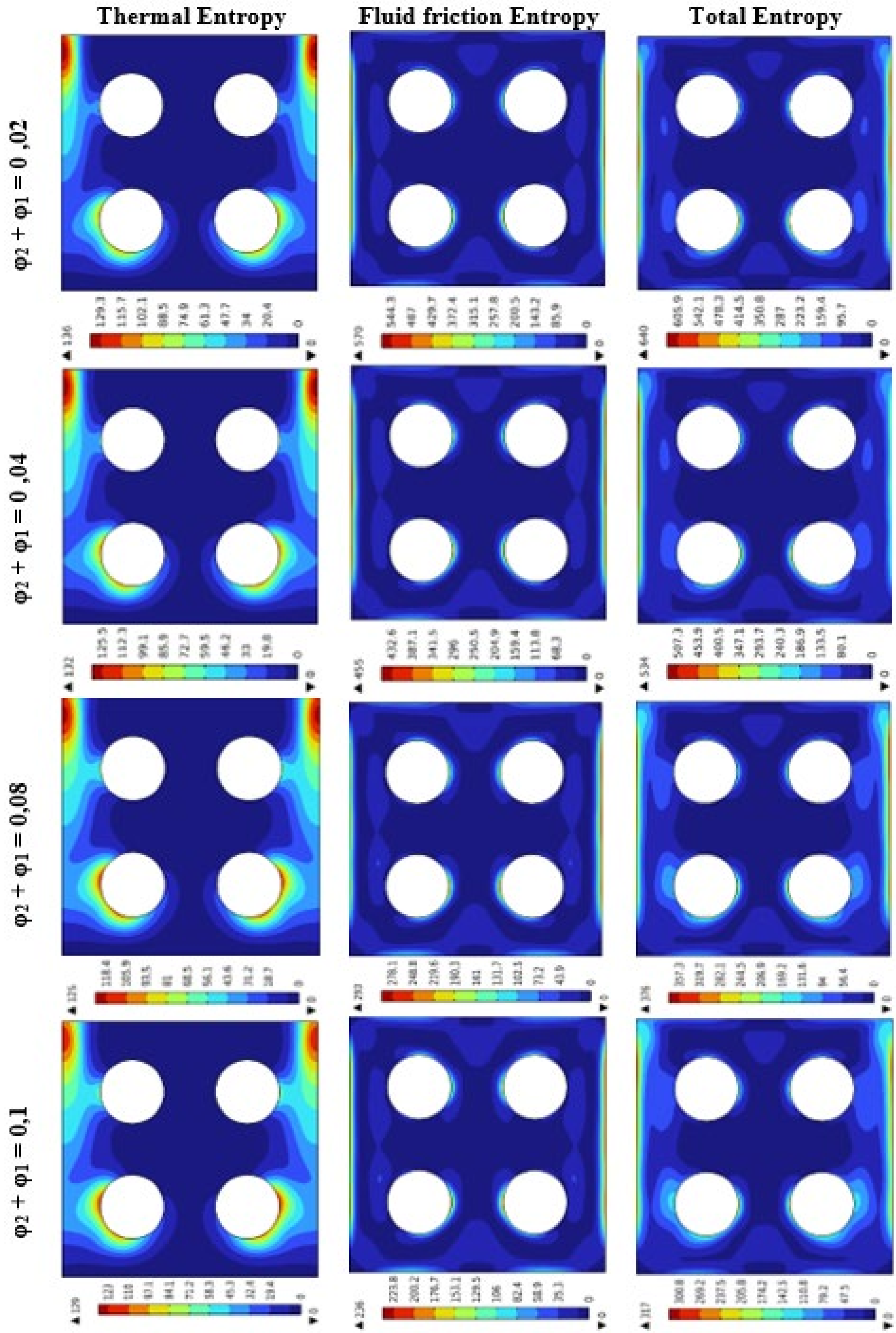

Fig. 14. Thermal, hydrodynamic and generated entropy contours for different volume fractions of hybrid nanoparticles at Ra = 10^5, Pr = 6.8, Ha = 0, γ = 0°, and L/H = 0.2.

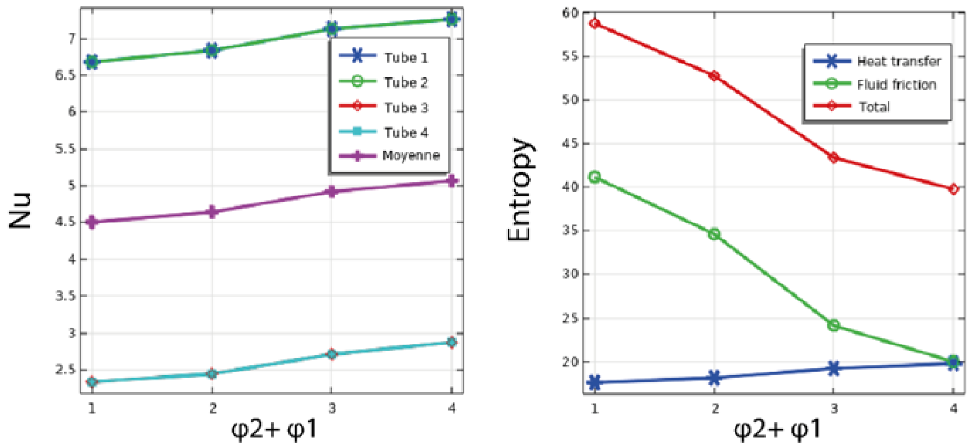

(a) Nusselt number (b) Entropy

Fig. 15. Variation of average Nusselt number for each tube and different average entropies for different volume fractions of hybrid nanoparticles at Ra = 10^5, Pr = 6.8, Ha = 0, $\gamma = 0°$, and L/H = 0.2.

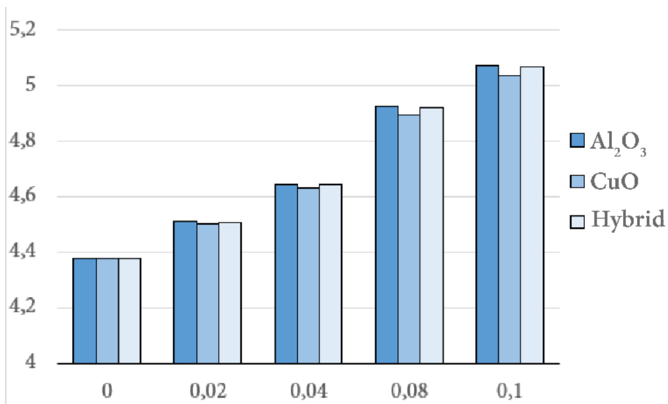

Fig. 16. Histogram comparing average Nusselt number for different nanoparticles, including hybrid, at different volume fractions at Ra = 10^5, Pr = 6.8, Ha = 0, $\gamma = 0°$, and $L/H = 0.2$.

However, it is important to consider other application-specific factors, such as nanofluid stability, cooling system compatibility and manufacturing constraints, before making a final decision (Table 6).

$\varphi_2 + \varphi_1$	0.00	0,02	0,04	0,08	0,1
Nu	4,3751	4.5076	4.6423	4.9211	5.0675
%Nu	--	3,0285	6,1072	12,479	15,825
Be	0.3008	0.2996	0.3437	0.4433	0.4977

Table 5. Average Nusselt number, percentage heat exchange and Bejan number for different volume fractions of hybrid nanoparticles at Ra = 10^5, Pr = 6.8, Ha = 0, $\gamma = 0°$, and $L/H = 0.2$.

Nanoparticles	Al_2O_3	CuO
Price in € /1kg	60 to 120	200 to 300

Table 6. Price of nanoparticles (2022).

5.4 Influence of the tubes radial disposition

In the final part of the present study, a proposed geometry that enhances heat transfer inside the heatsink has been presented. Therefore, the radial position of the four heatsink tubes has been varied, while adjusting the L/H form factor from 0.1 to 0.4, which represents the ratio between the distance separating the heatsink and its height.

The aim of this analysis is to assess the effect of these geometrical modifications on heatsink performance. By comparing the results obtained for each configuration, we will seek to determine whether a specific configuration can lead to a significant improvement in cooling performance.

Figure 17 shows the velocity, streamline and temperature contours for four proposed configurations, where the L/H form factor varies from 0.1 to 0.4. Analyzing the velocity contours for the different heatsink configurations, a decrease in flow velocity can be observed as passing from the closely-spaced to the far-spaced tube arrangement. This reduction is due to the narrowing of fluid flow cross-sections in the case of a closely spaced configuration. In this configuration, the tubes are placed closer together, creating narrower passages. In the far -spaced configuration, the tubes are spaced further apart, allowing to greater fluidity of the nanofluid circulation through wider passage cross-sections.

Looking at the streamlines in Fig. 17, it can be seen that as the tubes are moved further apart, two vortices of increasing size are created between the upper and lower tubes. This observation suggests a significant change in the structure of the fluid flow. In the close-tube configuration, the streamlines show a more intense interaction between the tubes, forming vortices of smaller size and limited dimension. In contrast, in the widely spaced tube configuration, the streamlines reveal the formation of two larger vortices between the upper and lower tubes. This allows the fluid to flow more fluency, creating hence larger vortex structures.

As for thermal distribution in the different heatsink configurations, there is a radical change when the tubes are moved further apart. In particular, the buoyancy effect decreases significantly. When the tubes are placed closer together in the standard configuration, the buoyancy effect is more pronounced, as the upward movement of the hot fluid and the downward movement of the cold fluid between the tubes create a natural circulation. However, by moving the tubes further apart, the space between them increases, reducing the interaction between upward and downward stream.

The entropy distribution illustrated in Fig. 18 shows a non-uniform behavior of the maximum value for each process. For this reason, a more detailed analysis based on its global average can clarify its variable behavior. Indeed, the curves in Fig. 19 (b) show that the average entropy due to heat transfer increases as the form factor increases. However, the mean entropy due to fluid friction increases as the form factor increases from 0.1 to 0.2, beyond which it begins to decrease with an overall predominance for form factors below 0.3 (see Bejan number, Table 7). On the other hand, the predominance of entropy due to heat transfer is noted beyond this factor, maintaining the overall decrease. This means that the far-spaced tube position globally prevents global irreversibility by shifting to a more ordered state.

In Fig. 19 (b), analysis of the Nusselt distribution in the four heatsink tubes, as a function of form factor, reveals an interesting trend. Moving from a closely-spaced tube configuration to a far-spaced tube configuration, an increase in the number of Nusselt, particularly in the top two tubes has been observed. This increase in Nusselt number indicates an improvement in overall heat transfer. By moving the tubes further apart, the increased space between them allows for a better fluid circulation and increased fluid-hot material interactions. This promotes more efficient heat dissipation, leading to an increase in the Nusselt number.

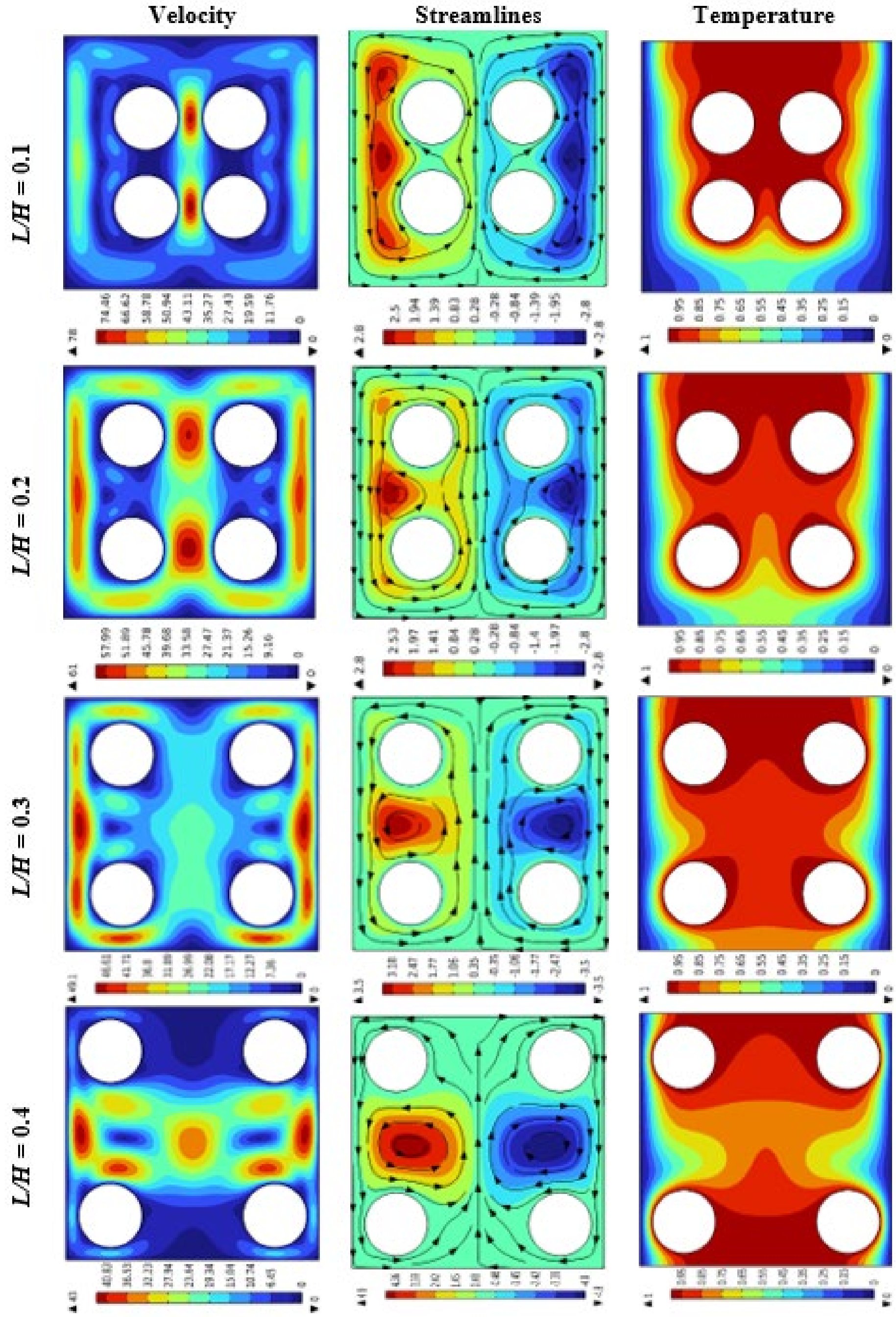

Fig. 17. Velocity contours, streamlines and temperature contours for different form factors at Ra = 10^5, Pr = 6.8, Ha = 0, $\gamma = 0°$, $\varphi_1 = \varphi_2 = 0.02$.

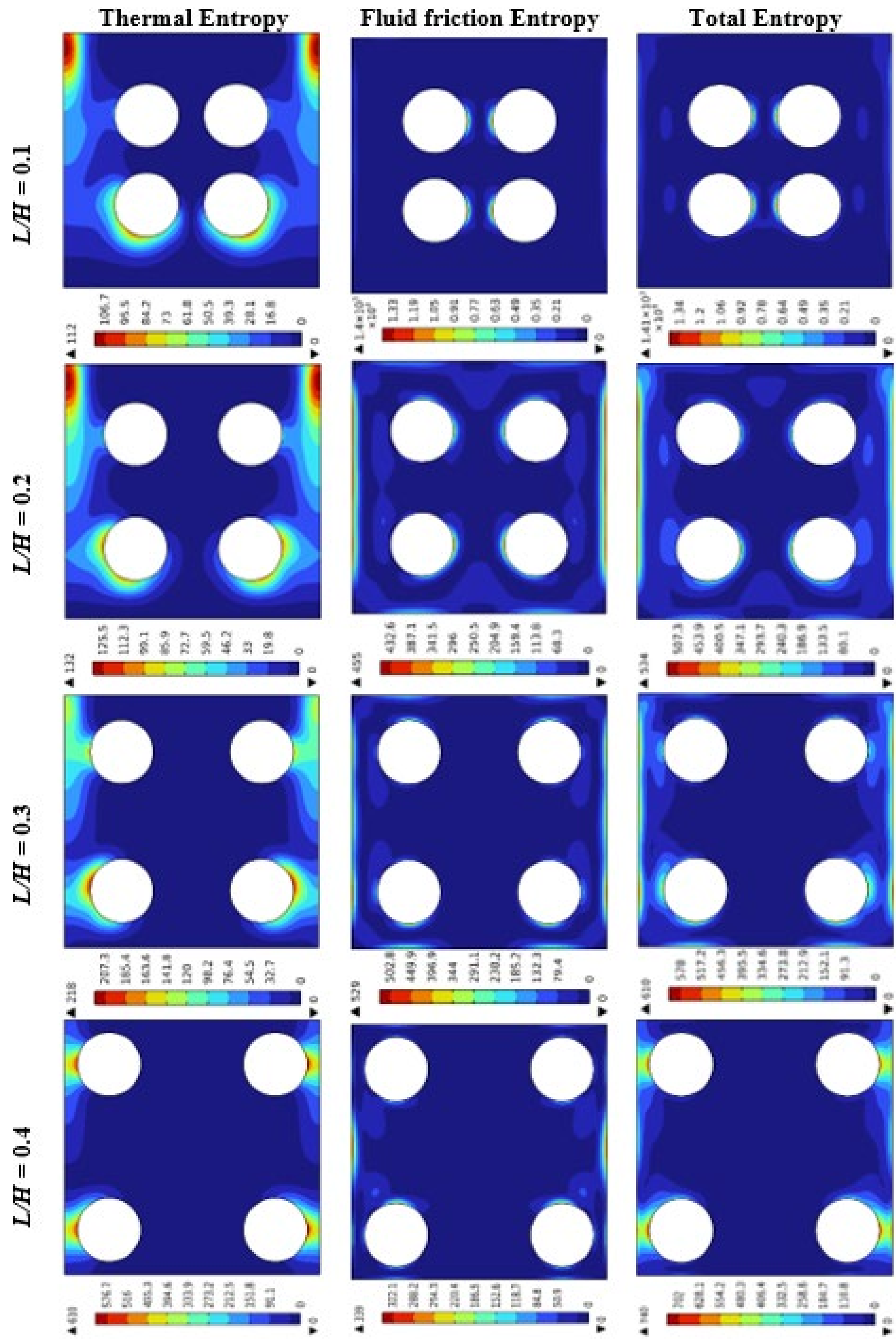

Fig. 18. Thermal, hydrodynamic and generated entropy contours for different form factors at Ra = 10^5, Pr = 6.8, Ha = 0, $\gamma = 0°$, $\varphi_1 = \varphi_2 = 0.02$.

On the other hand, lowering the lower tubes reduces buoyancy heat build-up in the upper tubes, so the cooling rate for these two tubes increases. Furthermore, based on the data in Table 7, the far-spaced configuration with a form factor of 0.4 resulted in a significant improvement in cooling, with a percentage improvement of up to 73% compared to the standard configuration. This improvement is remarkable and demonstrates the effectiveness of this configuration in dissipating heat more efficiently.

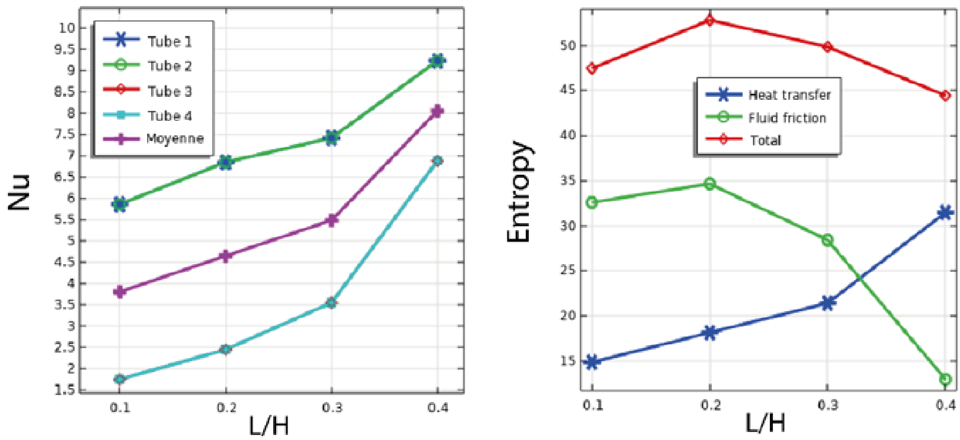

(a) Nusselt number (b) Entropy

Fig. 19. Variation in average Nusselt number for each tube and different average entropies for different radial arrangements at Ra = 10^5, Pr = 6.8, Ha = 0, $\gamma = 0°$, $\varphi_1 = \varphi_2 = 0.02$.

L/H	0,1	0.2	0.3	0.4
Nu	3.79975	4.64237	5.47858	8.04742
%Nu	-18,150	--	18,012	73,347
Be	0.313085	0.343761	0.429825	0.708324

Table 7. Average Nusselt number, percentage of heat exchange and Bejan number for different radial arrangements at Ra = 10^5, Pr = 6.8, Ha = 0, $\gamma = 0°$, $\varphi_1 = \varphi_2 = 0.02$.

6. Conclusion

In this investigation, an in-depth study to improve the thermal performance of a heatsink through several aspects has been presented. The effects of nanoparticle, magnetic field, buoyancy and geometry on CPU heatsink performance have been highlighted. The main points to be concluded from this study are as follows:

The increase in CPU temperature leads to an increase in the flow velocity of the hybrid nanofluid, promoting better heat transfer. The thermal profile shifts upwards, indicating better heat dissipation at the bottom of the block.

The presence of a magnetic field leads to a significant reduction in the heat sink's cooling capacity, accompanied by an increase in entropy due to fluid friction. The effect of the magnetic field disrupts nanofluid flow rates, reducing heat transfer efficiency.

The addition of nanoparticles, particularly alumina, improves heat transfer overall, with an increase in the Nusselt number. Nanoparticle hybridization shows similar results to increasing the concentration of individual nanoparticles.

Moving the tubes further apart in the heatsink configuration has a significant effect on cooling, with a marked improvement in heat transfer by increasing the form factor and moving the tubes further apart. This promotes better nanofluid circulation and reduces overall entropy generation, leading to more efficient heat dissipation.

By combining the aspects of using a water- and Al2O3-based nanofluid with a far-spaced configuration, designers can benefit from both a high heat transfer rate and reduced entropy generation. This will help improve CPU cooling performance, maintaining optimum operating temperatures and reducing the risk of overheating.

These results provide important information for CPU cooling system optimization, highlighting the importance of parameters such as temperature, magnetic field, nanoparticles and geometrical configuration. This knowledge can be used to design more efficient heat sinks and improve the cooling performance of electronic devices.

Nomenclature

Symbol		y	Vertical coordinate
B	Magnetic flux density	Y	Dimensionless vertical y
Be	Bejan number	Greek	
Cp	Heat capacity	α	Thermal diffusivity
D	Tube diameter	β	Thermal expansion
F	Volume force	γ	Magnetic field angle
g	Gravity acceleration	ε	Computation error
H	Bloc height	Θ	Dimensionless temperature
Ha	Hartmann number	μ	Dynamic viscosity
k	Thermal conductivity	ρ	Density
l	Distance	σ	Electric conductivity
L	Distance between tubes	φ	Volume fraction
ℓ	Curvilinear abscissa	Φ	Dependent variable
Lo	Bloc length	χ	Entropy factor
n	Normal coordinate	Ψ	Dimensionless stream function
N	Dimensionless normal coordinate	Subscript	
Nu	Nusselt number	nf	Nanofluid
p	Pressure	p	Nanoparticles
P	Dimensionless pressure	f	Base fluid
Pr	Prandtl number	h	Hot
q	Surface heat flux	c	Cold
Ra	Rayleigh number	CuO	Copper oxide
s	Entropy	Al_2O_3	Alumina
S	Dimensionless entropy	x	According to x
T	Temperature	y	According to y
u	Horizontal velocity	l	Local
U	Dimensionless horizontal u	gen	Generated
v	Vertical velocity	HT	Heat transfer
V	Dimensionless vertical v	FF	Fluid friction
x	Horizontal coordinate	Superscript	
X	Dimensionless horizontal x	n	Iteration

References:

Alsarraf J, Shahsavar A, Khaki M, Ranjbarzadeh R, Karimipour A, Afrand M (2020). Numerical investigation on the effect of four constant temperature pipes on natural cooling of electronic heatsink by nanofluids: a multifunctional optimization. Advanced Powder Technology, 31(1), 416-432.

Anouar Y, Mokhefi A (2022). Numerical investigation of the nanofluid natural convection flow in a CPU heatsink using Buongiorno two-phase model. Journal of the Serbian Society for Computational Mechanics, 16(2), 13-42.

Brinkman HC (1952). The viscosity of concentrated suspensions and solutions. J. Chem. Phys, 20, 571-581.

Buongiorno J (2006). Convective transport in nanofluids. Journal of Heat Transfer, 128(3), 240-250.

Dechaumphai P (1999). Finite Element Method in Engineering, second ed, Chulalongkorn University Press, Bangkok.

Keblinski P, Eastman JA, Cahill DG (2005). Nanofluids for thermal transport. Materials Today, 8(6):36-44.

Lau MC, Srinivasan R (2016). A hybrid CPU-Graphics Processing Unit (GPU) approach for computationally efficient simulation-optimization. Computers & Chemical Engineering, 87, 49-62.

Maxwell JC (1881). A Treatise on Electricity and Magnetism, vol. II, Oxford University Press, Cambridge, UK, 1873. p. 54.

Moghadasi, H., Aminian, E., Saffari, H., Mahjoorghani, M., & Emamifar, A. (2020). Numerical analysis on laminar forced convection improvement of hybrid nanofluid within a U-bend pipe in porous media. International Journal of Mechanical Sciences, 179, 105659.

Mokhefi A, di Schio ER (2022). Effect of a magnetic field on the couette forced convection of a buongiorno's nanofluid over an embedded cavity. JP Journal of Heat and Mass Transfer, 30, 89-104.

Naphon P, Wiriyasart S (2009). Liquid cooling in the mini-rectangular fin heatsink with and without thermoelectric for CPU. International Communications in Heat and Mass Transfer, 36(2), 166-171.

Park SE, Jung JY (2019). Thermal conductivity enhancement of hybrid nanofluids and their application in microchannel heatsinks. International Journal of Heat and Mass Transfer, 132, 729-739.

Raj CP, Suresh S, Rajan KS (2019). Experimental investigations on the heat transfer and rheological behavior of hybrid nanofluids. Journal of Thermal Analysis and Calorimetry, 135(1), 543-552.

Ranga Babu JA, Kiran Kumar K, Srinivasa Rao S (2017). State-of-art review on hybrid nanofluids. Renewable and Sustainable Energy Reviews, 77, 551-565.

Rossi di Schio E, Impiombato AN, Mokhefi A, Biserni C (2022). Theoretical and Numerical Study on Buongiorno's Model with a Couette Flow of a Nanofluid in a Channel with an Embedded Cavity. Applied Sciences, 12(15), 7751.

Shahsavar A, Entezari S, Askari IB, Ali HM (2021). The effect of using connecting holes on heat transfer and entropy generation behaviors in a microchannels heatsink cooled with biological silver/water nanofluid. International Communications in Heat and Mass Transfer, 123, 104929.

Shahsavar A, Moradi K, Yıldız Ç, Farhadi P, Arıcı M (2022). Effect of nanoparticle shape on cooling performance of boehmite-alumina nanofluid in a helical heatsink for laminar and turbulent flow regimes. International Journal of Mechanical Sciences, 217:107045.

Siricharoenpanich A, Wiriyasart S, Srichat A, Naphon P (2019). Thermal management system of CPU cooling with a novel short heat pipe cooling system. Case Studies in Thermal Engineering, 15:100545.

Siricharoenpanich, A., Wiriyasart, S., Srichat, A., & Naphon, P. (2019). Thermal management system of CPU cooling with a novel short heat pipe cooling system. Case Studies in Thermal Engineering, 15, 100545.

Taylor C, Hood P (1973). A numerical solution of the Navier-Stokes equations using the finite element technique. Computers & Fluids, 1(1), 73-100.

Tzou GJ, Tsao CC, Lin YC (2010). Improvement in the thermal conductivity of aluminum substrate for the desktop PC Central Processing Unit (CPU) by the Taguchi method. Experimental thermal and fluid science, 34(6), 706-710.

Wang H, Pang M, Diao Y, Zhao Y (2022). Heat transfer characteristics and flow features of nanofluids in parallel flat minichannels. Powder Technology, 402, 117321.

Xiahou G, Zhang J, Ma R, Liu Y (2019). Novel heat pipe radiator for vertical CPU cooling and its experimental study. International Journal of Heat and Mass Transfer, 130, 912-922.

Xie H, Wang J, Xi T, Liu Y (2002). Thermal conductivity of suspensions containing nanosized SiC particles. International Journal of Thermophysics, 23(2), 571-580.

Yang Y, Hu W, Chen X, Cao G (2018). Energy-aware CPU frequency scaling for mobile video streaming. IEEE Transactions on Mobile Computing, 18(11), 2536-2548.

Zhao N, Qi C, Chen T, Tang J, Cui X (2019). Experimental study on influences of cylindrical grooves on thermal efficiency, exergy efficiency and entropy generation of CPU cooled by nanofluids. International Journal of Heat and Mass Transfer, 135, 16-32.